

Sensitivity of Rotorcraft Hover Predictions to Mesh Resolution in Strand Grid Framework

VINOD LAKSHMINARAYAN¹, JAYANARAYANAN SITARAMAN², AND ANDREW WISSINK³

¹Science & Technology Corporation, NASA Ames Research Center, Moffett Field, CA

²Parallel Geometric Algorithms LLC, Sunnyvale, CA

³US Army Aviation Development Directorate - AFDD (AMRDEC), Moffett Field, CA

The strand grid approach is a flow solution method where a prismatic-like grid using “strands” is grown to a short distance from the body surface to capture the viscous boundary layer and the rest of the domain is covered using an adaptive Cartesian grid. The approach offers a potential for nearly automatic grid generation and adaptation requiring very few input parameters; at same time offering the ability to obtain fast and efficient flow solution. This paper explores the sensitivity of rotor hover predictions to various meshing parameters in the strand grid framework. Surface mesh resolution has minimal impact on the predictions, whereas both the outer extent of the strand mesh and the Cartesian mesh resolution have significant effect to rotor performance and wake predictions. A strand mesh extending out to half a chord distance away and a Cartesian mesh spacing of less than two times the outer boundary spacing of the strand mesh is recommended for most rotor blade simulations.

I. Introduction

The ability to accurately predict the hover performance of a rotor is critical in rotary-wing vehicle design. For a full-scale helicopter rotor a 1% change in figure of merit (a commonly used measure of rotor efficiency) can translate to 200-300 lb of useful payload. With the advances in high performance parallel computing power over the past decade, high fidelity Computational Fluid Dynamics (CFD) analyses of helicopter rotors in hover have now become routine.¹⁻³ However, as the AIAA Hover Prediction Workshop results have shown,⁴ there is still considerable variation in the results depending on the code and the meshes used.

Traditionally, there are two primary types of flow solvers available: structured grid solvers and unstructured grid solvers. Structured grid solvers are efficient and allow use of higher order algorithms. The efficiency of structured grid solvers enables use of many more grid points to provide accurate solution. However, generating a structured grid, even when using multi-block structured and/or overset meshes, can be extremely challenging. On the other hand, unstructured codes generally offer more flexibility and automation in grid generation and problem setup for geometrically-complex bodies such as fuselages and hubs. But, the overall computational cost associated with such solvers to provide comparative level of accuracy as a structured grid solver is significantly higher.

The strand grid approach^{5,6} provides the potential for performing high-fidelity modeling and simulation with a very high degree of automation while achieving a solver efficiency comparable to structured grid solvers. In this approach, the volume mesh generation process is fully automated by extending a viscous-quality prismatic mesh directly from a surface tessellation composed of triangles and quadrilaterals. A near-body volume grid that resolves the

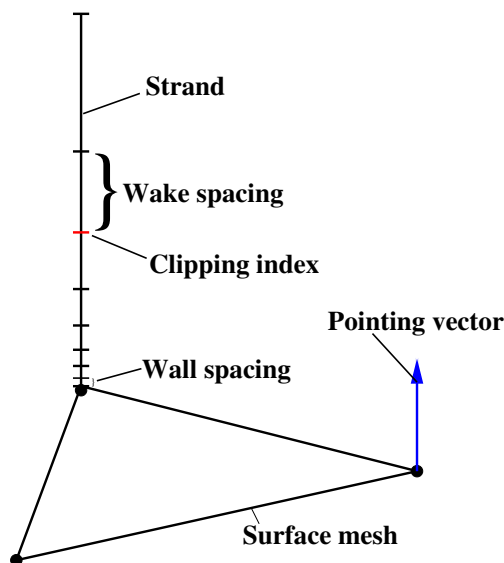


Figure 1. Strand definition.

viscous boundary layer is constructed by inflating the surface grid along curves that can be represented with just a few parametric quantities. These curves, referred to as “strands”, are straight lines in most regions, each represented by a pointing vector and a length (see Fig. 1). Strands extrude a short distance from the solid boundary and intersects with adaptive Cartesian grids, which cover the rest of the domain to the outer boundaries. The strand and the Cartesian grids are connected through an overset interface. The Cartesian grid is automatically generated based on the wake spacing of the strand grid.

The objective of this work is to assess the sensitivity of rotor hover predictions to the few independent meshing parameters in the strand grid framework. Specifically, the sensitivity of the rotor performance and the tip vortex/wake characteristics to these parameters will be analysed. The intention of this work is to provide a best-practice guideline for researchers using strand grid framework to simulate rotorcraft problems.

The mesh generation in the strand grid framework requires the following inputs: 1) a surface tessellation, which can be composed of either triangles or quadrilaterals or a mix of both, 2) a strand length, which determines the outer extent of the strand grid, 3) a wall spacing to achieve a desired $y+$, 4) a desired wake spacing, which is the normal spacing at the strand outer boundary, and 5) a ratio of the near-body to the off-body mesh resolution at the overset interface. Among these parameters, the viscous wall spacing is determined by the flow Reynolds number and is typically fixed for a particular problem. The wake spacing to some extent is determined by the strand length and a desired stretch ratio. Therefore, the two independent parameters that can be varied in the near-body mesh for a given problem are the surface tessellation and the strand length. Further, the finest level spacing of the off-body Cartesian grid is determined by the ratio of the off-body to the near-body mesh resolution at the overset interface. In this work, this ratio is also considered an independent parameter to identify the sensitivity of the simulation to the off-body grid and the overset interfacing.

All the simulations in this work are performed using the Helios software,^{7–9} which is a rotary-wing product of the HPCMP CREATETM-AV (air vehicles) program.¹⁰ Helios incorporates the strand grid approach as one of the options to perform high-fidelity CFD analysis. Helios uses mStrand¹¹ as the specialized strand grid solver to resolve near-body viscous region and SAMCart³ as the block structured Cartesian solver in the off-body to resolve the wake through a combination of high-order algorithms and adaptive mesh refinement (AMR). The PUNDIT¹² domain connectivity software facilitates parallel data exchange between the two mesh types as well as enables relative motion between the mesh systems. Coordination of the different codes is managed through a lightweight and flexible Python-based infrastructure.^{13,14}

The remainder of the paper is organized as follows. Section II provides a brief description of the flow solvers. This is then followed by a description of the mesh generation strategies used in this work in Section III. Results from earlier validation studies using the strand grid framework is presented in Section IV. The results showing the sensitivity of rotor hover predictions to strand meshing parameters is provided in Section V. Concluding remarks are offered in Section VI.

II. Description of Flow Solvers

This section provides a brief description of the near-body strand solver, mStrand,¹¹ and the off-body Cartesian solver, SAMCart.³

II.A. Strand Near-Body Solver (mStrand)

mStrand is a newly developed specialized strand grid solver that uses a vertex-centered finite-volume spatial discretization. The Reynolds-averaged Navier-Stokes (RANS) equations in a general moving coordinate system in three dimensions is solved. mStrand accommodates both quadrilateral and triangular surface elements and handles general prismatic meshes in the normal (strand) direction. The Roe’s approximate Riemann solver¹⁵ is used to compute the inviscid conservative fluxes. The second-order gradients are limited using a differentiable form of Van-Albada’s limiter¹⁶ in both the streamwise and the strand directions. The solver incorporates a second-order implementation of full Navier-Stokes for the viscous terms (no thin-layer approximation) and the Spalart-Allmaras turbulence model¹⁷ with first order discretization. Implicit solution is performed using a fully coupled (mean-flow and turbulence equations) preconditioned GMRES.¹⁸ A specialized strand-based preconditioner is constructed from first-order Jacobian terms that require only nearest neighbor contributions. A fully parallel implementation of mStrand is obtained by partitioning the surface mesh into contiguous blocks on the basis of surface elements using Metis.¹⁹ More details of the

mStrand solver can be found in Ref. 11.

II.B. Cartesian Off-body Solver (SAMCart)

A structured adaptive solver SAMCart is used for the Cartesian off-body grid. The parallel mesh adaptive capability is provided by the SAMRAI²⁰ library and the solution in each block is obtained using a solver called Cart. The Cart solver uses a high-order central differencing scheme - 6th order with 5th order dissipation for the inviscid terms and 4th order for the viscous terms. Cart implements the Spalart-Allmaras turbulence model and can also enable DES capability. The solver includes an implicit second order BDF2 time integration scheme with LU-SGS and diagonalized ADI implicit operators. Further description of SAMCart can be found in Refs. 21 and 22.

III. Mesh Generation

This sections provides details regarding the strand and the Cartesian mesh generation strategies.

III.A. Strand Mesh

All the strand meshes used in this work are generated using a code called mStrandGen (multi-Strand Mesh Generator). The algorithm used in mStrandGen was first introduced in Ref. 23. The inputs for the strand mesh generation are 1) a surface tessellation, which can be composed of triangles and quadrilaterals, 2) a strand length, 3) a wall spacing to achieve a desired y^+ , and 4) a desired wake spacing. The desired wake spacing correlates to the finest spacing in the Cartesian grid used to resolve the wake.

While generating a strand mesh, strands are grown from each surface vertex. The initial strand direction vector is constructed by computing the average face normals of the elements that share the vertex. All strands have same number of points and point distribution; so they grow to an identical length that depends on the input parameters. Spacing along each strand ranges from viscous at the root to a specified wake spacing at the outer extent, as shown in Fig. 1.

Next, smoothing is applied to improve coverage and mesh quality around sharp corners, such as the leading or trailing edges. A smoothing algorithm is applied which seeks to average each strand direction vector relative to its neighbors, effectively seeking isotropic spacing in the prism cells at the strand extents. Figure 2 shows a comparison of a non-smoothed and a smoothed mesh. Smoothing is implemented using an iterative scheme such that the degree of smoothing can be adjusted by the number of iterations. In general it is desirable to have a maximally smoothed strand mesh to yield isotropic cells at the strand extents that transition smoothly to the Cartesian off-body mesh. In practice, however, there are circumstances where too much smoothing produces negative volumes in the prism stack due to strand crossings. To avoid this issue, smoothing is applied in an iterative fashion whereby the maximal smoothing is applied that does not result in strand crossings. That is, after each smoothing iteration prism volumes are computed and smoothing is stopped if any negative volumes are found.

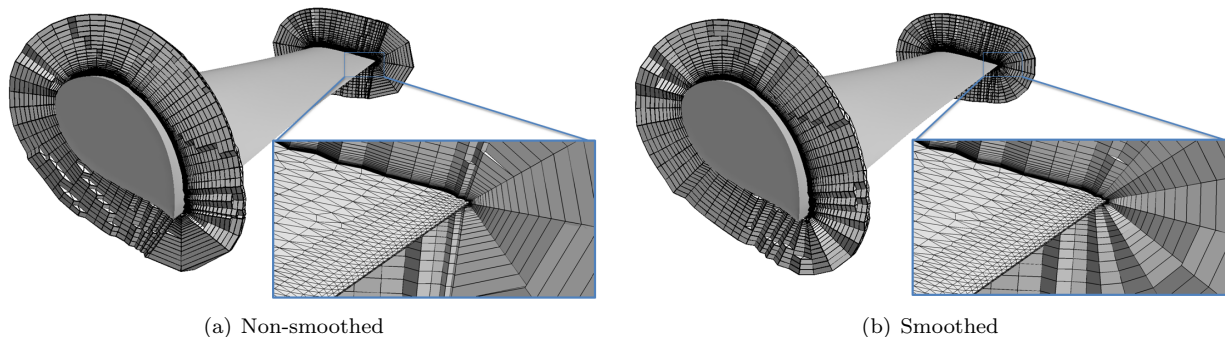


Figure 2. Strand direction vector smoothing. (a) initial direction vector normal to surface, no smoothing applied, (b) strands with smoothed direction vectors.

To improve the overall mesh quality, a multi-level strand mesh generation strategy is used. This strategy grows strands in multiple levels, typically three or four. The steps for generating the first level is exactly identical to that described above, but the strands are now grown only to a fraction of the specified final distance. In the subsequent levels, the tessellation of the inflated surface from the previous level is used as the starting point and strands are grown further outward. The strands generated with this approach are not necessarily a straight line, but are made up of few line segments. However, the requirement of having a compact representation of the strands is still valid. Figure 3 shows an example of a multi-level strand mesh by plotting a section of the mesh near the tip of a blade.

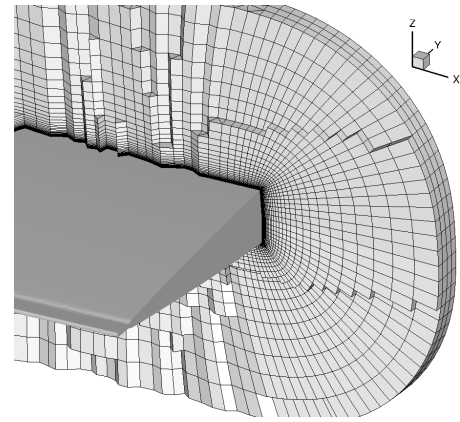


Figure 3. Multi-level strand mesh near the tip of a blade.

III.B. Cartesian Mesh

The Cartesian grid is generated following a Berger and Colella²⁴-style multi-level block-structured AMR (SAMR) grid hierarchy. The coarsest level defines the physical extent of the computational domain and new levels are constructed from coarsest to finest. Each finer level is formed by selecting cells on the coarser level and then clustering the marked cells together to form block regions that will constitute the new finer level. The result is a hierarchy composed of nested refinement levels, with each level formed as a union of logically-rectangular grid regions.

The Cartesian grid is refined to match specified mesh spacing ratio, α , at the extents of the strand mesh, as demonstrated in Fig. 4. The location of the clip index elements (x, y, z) and the wake spacing Δs are provided to the Cartesian grid generator (a), cells on the Cartesian grid system that contain strand outer boundary elements are checked (b) to see whether the Cartesian grid spacing Δx is greater than the specified factor of the wake spacing $\alpha \Delta s$. If they are, $\Delta x > \alpha \Delta s$, the Cartesian cell is marked for refinement. All marked cells are clustered to construct a new finer level in the hierarchy. The process is repeated until no Cartesian cells are marked, fully satisfying overset donor-receiver requirements and ensuring good mesh overlap at the Strand/Cartesian overset boundary.

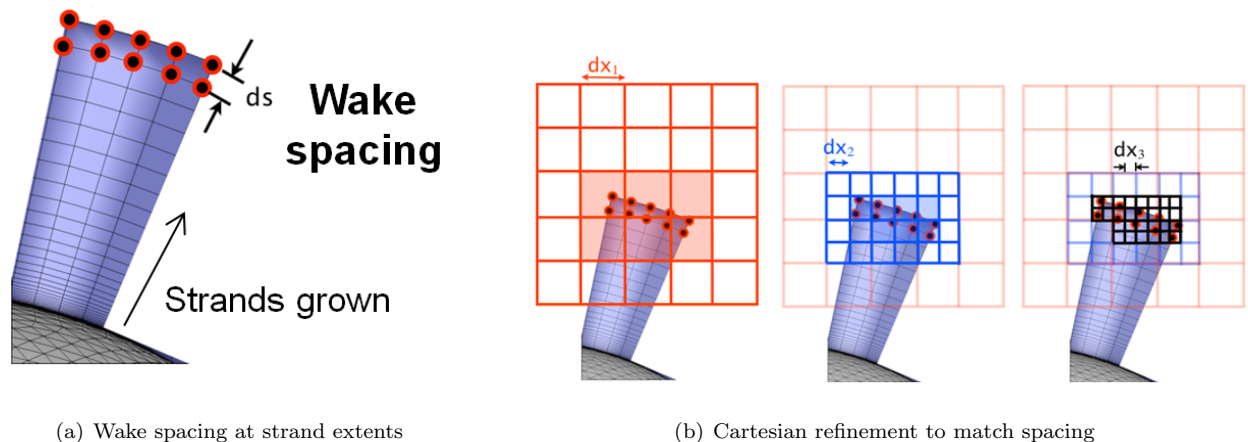


Figure 4. Off-body adaptive Cartesian mesh generation to resolve overset interface between strand and Cartesian grids.

After the initial generation of adaptive Cartesian grids to satisfy geometric requirements, grids are subsequently adapted throughout the simulation. Mesh cells that contain regions of swirling flow are identified using the scaled Q-criteria scheme proposed by Kamkar et al.²⁵ Alternative solution quantities – e.g., vorticity or Q-criteria magnitude, density variation, entropy, etc. – could readily be substituted to drive refinement in the adaptive solution procedure. However, the scaled Q-criterion automates the wake refinement procedure, which is an advantage over other quantities. If a defined quantity such as vorticity or Q criteria is used, predicting beforehand the appropriate threshold is often difficult. Also, the strength of the vortex wake may be variable throughout the simulation. Multiple runs are therefore required to determine a suitable threshold quantity. The scaled Q quantity requires no such tuning and automatically adjusts to the changing scales of rotational flow in the wake.

IV. Validation

This section demonstrates the ability of the strand grid framework to accurately predict rotor hover performance as well as tip vortex formation and evolution. The results shown in this section were originally presented in an earlier work by the current authors.¹¹

IV.A. TRAM Rotor in Hover

The performance prediction capability of the strand grid framework is demonstrated using (TRAM) rotor, which is a quarter-scale model of the right-hand Bell/Boeing V-22 three-bladed proprotor tested in the Duits-Nederlandse Windtunnel Large Low-speed Facility (DNW-LLF). Computed results are compared to the hover tests conducted in airplane mode at tip Mach number 0.62. Aerodynamic surface pressures, thrust and power, were measured along with structural loads and aeroacoustics data. A summary of the nominal operating conditions used for the computational model are shown in Table 1. Further details of the test are given in a comprehensive report by Johnson.²⁶

Tip chord c	5.5 in
Blade radius R	57 in
Tip Mach number M_{tip}	0.62
Re number at tip Re_{tip}	2.1×10^6

Table 1. Nominal operating conditions for isolated TRAM rotor studies.

Figure 5 shows the variation of power coefficient (C_Q) with thrust coefficient (C_T), normalized by the rotor solidity (σ) and the variation of figure of merit ($FM = C_T^{3/2} / (\sqrt{2}C_Q)$) with C_T , obtained by changing the collective angle of the blade. Plotted are the results from the experiments, Helios/mStrand setup and the results obtained using an unstructured near-body flow solver (NSU3D²⁷) in the Helios framework.²⁸ The Helios/NSU3D calculation is considered the benchmark best results obtained for this rotor with the Helios framework. The results clearly show that the performance predicted by the strand grid framework is comparable to the best available predictions. Both the CFD calculations under-predict the FM by 2 – 3% at intermediate collective angles.

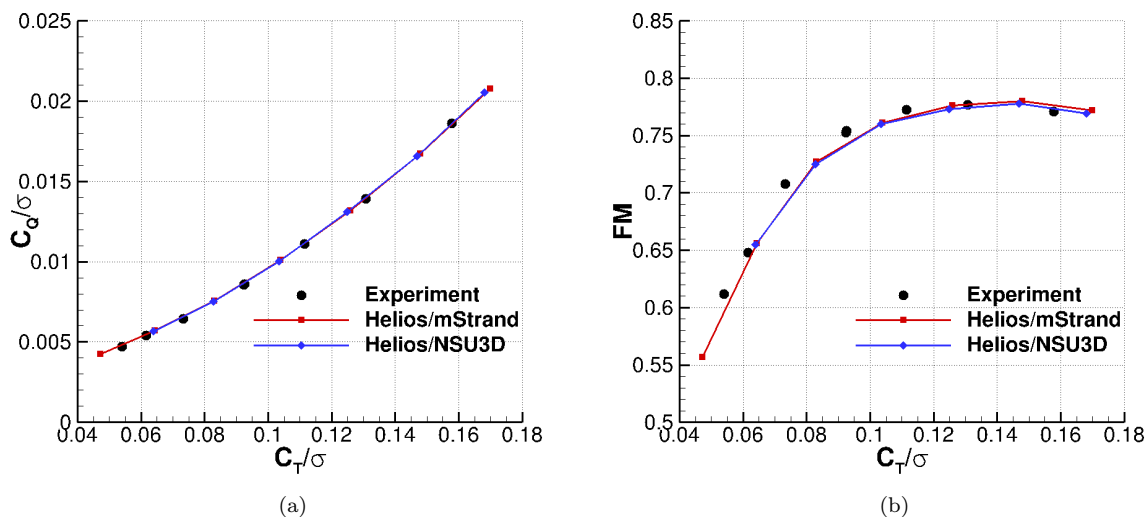


Figure 5. Performance results from TRAM rotor simulation.

IV.B. “Martin” Rotor in Hover

The results for the so-called “Martin” rotor²⁹ is used to demonstrate the ability of the strand grid approach to accurately predict tip vortex formation and evolution in hover. In the experiments, the tip vortex evolution

was studied using LDV-based velocity measurements made at selected wake planes ranging from 3 to 395 deg. The setup consisted of single untwisted blade with rectangular planform (with a square tip share) operated on a hover test stand. The relevant test-case details are given in Table 2.

Chord c	44.5 mm
Blade radius R	406 mm
Tip Mach number M_{tip}	0.26
Tip Reynolds number Re_{tip}	272,000
Collective pitch θ	4.5°
Root cutout	20%
Airfoil	NACA 2415

Table 2. Experimental test conditions for Martin rotor.

Figure 6(a) shows the streamwise vorticity contour near the tip of the blade at selected sections. The formation of tip vortex is very well resolved and the presence of secondary and tertiary vortices is evident. Similar conclusion can be drawn from Fig. 6(b), which shows the iso-surface of q -criterion colored by vorticity magnitude contours. The vortex is transferred smoothly from one mesh to the other. Also seen in this plot is the returning vortex after one blade passage. The twisting of the returning vortex is prominent. The off-body Cartesian mesh has refined adaptively to capture the wake.

Figure 7 provides a quantitative comparison of the captured wake with the experimentally measured swirl velocity (normalized by the rotational speed of the rotor) profile at different wake planes. The swirl velocity profile is obtained by cutting a horizontal line across the center of the vortex in that plane. The x -axis in these plots is the radial location of the vortex normalized by the blade radius. Therefore, the contraction of the wake with increasing wake age is reflected in these plots. The predicted contraction rate is accurate when compared to the experimentally measured value. Examining the vortex profiles, the peak swirl velocity is slightly under-predicted at the earliest wake age ($\xi = 3^\circ$), which probably results in a slightly larger vortex core. At this wake age, any discrepancy can be primarily attributed to the difficulty in accurately predicting the tip vortex formation using a RANS-based solver. Computational solutions of the RANS equations suffer from numerical and turbulence modeling errors, that can make the prediction of tip vortex formation extremely challenging. It should be noted that these predictions are as accurate or better than most results available in the literature.

At other wake ages shown, the tip vortex is resolved in the off-body Cartesian mesh. The high-order

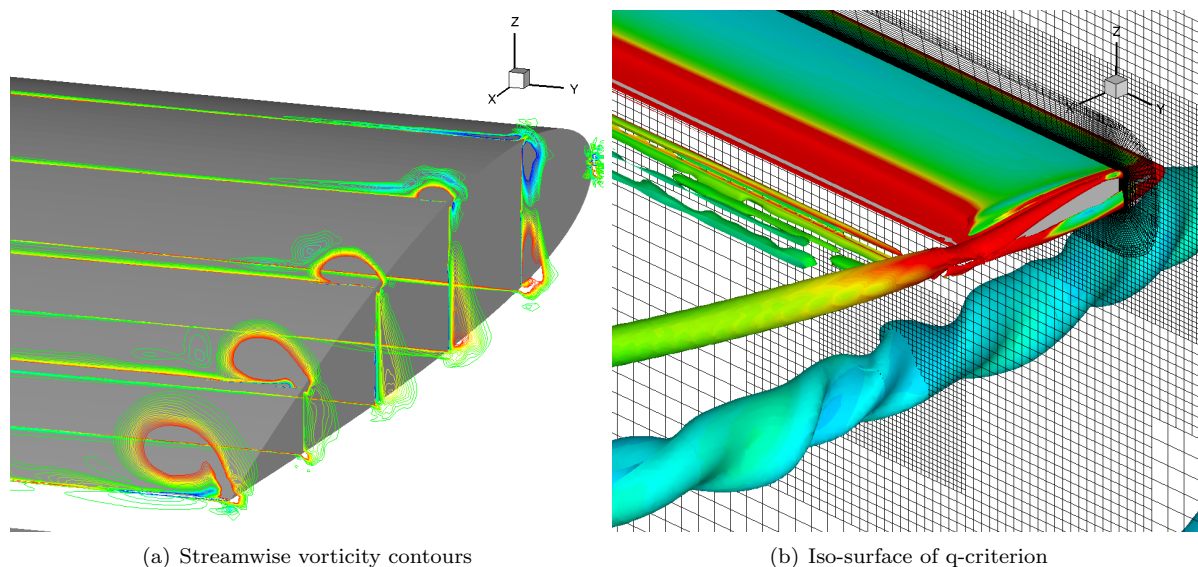


Figure 6. Formation of trailed vortex system in Martin rotor simulation.

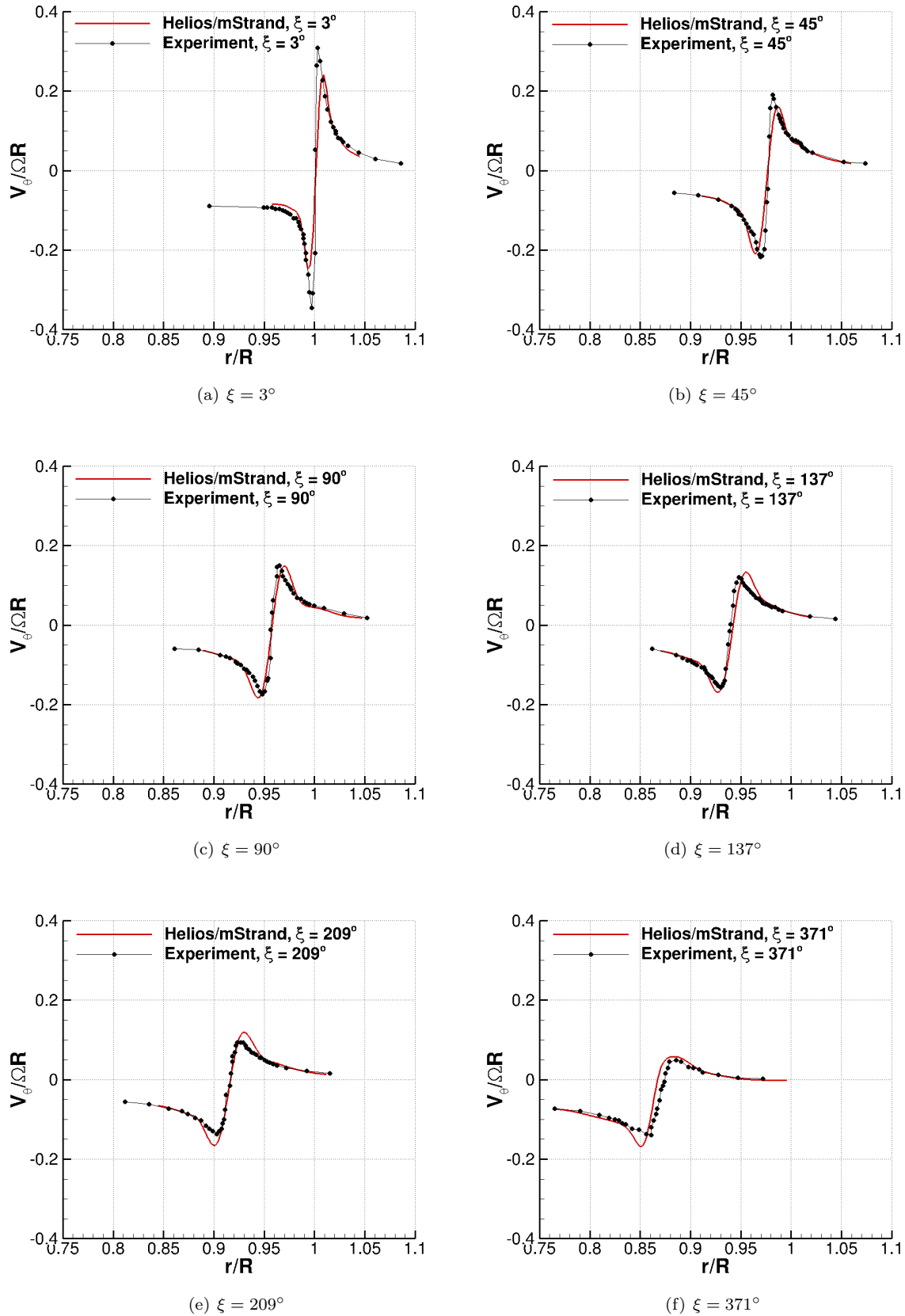


Figure 7. Swirl velocity comparison for Martin rotor simulation.

Cartesian solver is able to preserve the vortex accurately and the discrepancy between the measurement and the prediction is seen to reduce as the wake age increases. Note that due to the twisting of the tip vortex (see Fig. 6), the velocity profiles obtained along cuts in different axes are not identical. Some discrepancies in the results could be attributed to that. Overall, the results obtained are very satisfactory and demonstrate that use of a strand-based near body mesh with an off-body Cartesian mesh is a viable framework for accurate prediction of tip vortex formation and evolution.

V. Sensitivity Results

The sensitivity of rotorcraft hover predictions to different mesh input parameters in the strand grid framework is evaluated using hover calculations of the TRAM rotor presented in the previous section. The blades are set at a collective angle of 14° . All three rotors and the hub are meshed with independent strand meshes that overset with each other. The PUNDIT domain connectivity facilitates parallel data exchange between different near-body meshes. Figure 8(a) shows an example strand mesh used for the TRAM rotor calculation. The hub mesh is comprised only of triangular elements. The blade mesh is comprised mainly of quadrilateral elements with triangular elements only at the tip cap. The use of quadrilateral and triangular elements in appropriate regions provide a balance between flow solution accuracy and ease of meshing. Figure 8(b) shows interface between the blade, the hub and the Cartesian meshes.

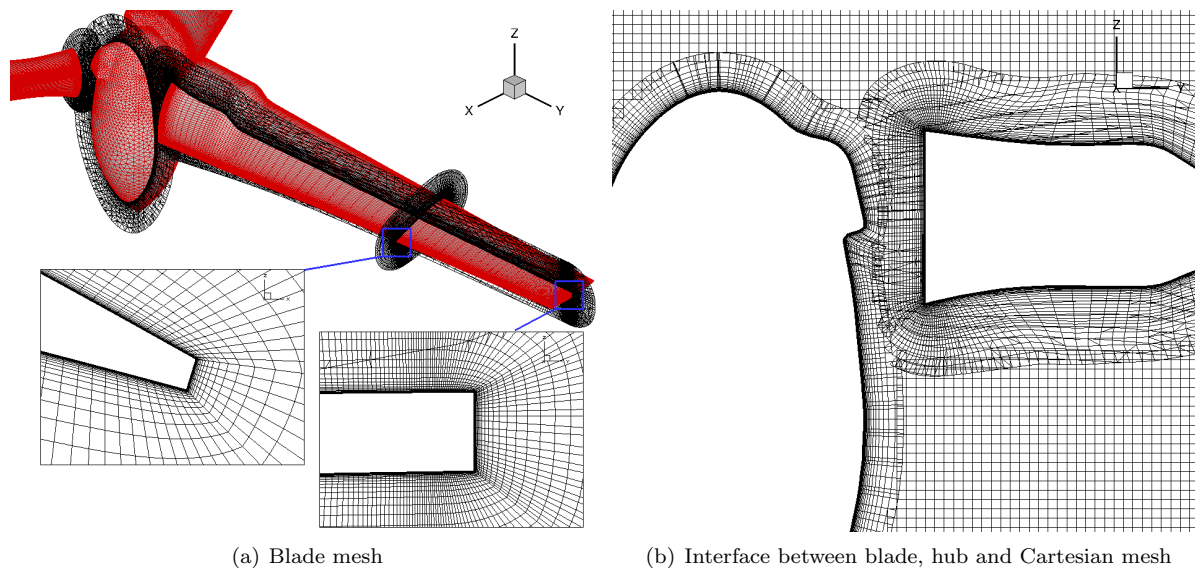


Figure 8. An example mesh for TRAM rotor simulation.

As mentioned before, the sensitivities to three parameters, namely, 1) surface resolution, 2) outer extent of the strand mesh (strand length), and 3) the Cartesian mesh resolution are investigated. All the calculations are run for 6 revs, 8640 steps with a rotor step of $\Delta\psi = 0.25^\circ$. The near-body solver uses 4 sub-iterations to obtain an order of magnitude of convergence in the residual while the off-body is run for 12 sub-iterations. Off-body AMR is turned on after two revs and adapted every 1.25° , or 5 time steps. Spalart-Allmaras turbulence model with rotational correction is used in both near- and off-body solvers.

V.A. Surface Resolution

To investigate the impact of surface resolution on the hover predictions, three different blade meshes are considered - coarse, intermediate and fine. Identical hub mesh is used in all cases. Table 3 provides the statistics of the different strand meshes. The only difference in the different blade meshes considered is the resolution near the tip region. The main motivation here is to understand the impact of mesh resolution near the tip on the predicted performance and wake characteristics. The coarse blade mesh has a resolution such that there are 10 points across the thickness of the blade, the intermediate resolution mesh has 20 points and the fine mesh has 40 points along the same length. In all the cases, a constant spacing with the

Mesh	Surface Nodes	Triangular Elements	Quadrilateral Elements	Strand Points
Coarse blade mesh	42808	8432	38590	101
Intermediate blade mesh	54712	9086	50167	101
Fine blade mesh	69109	10640	63787	101
Hub mesh	4495	8986	0	101

Table 3. TRAM near-body mesh statistics with different surface resolution.

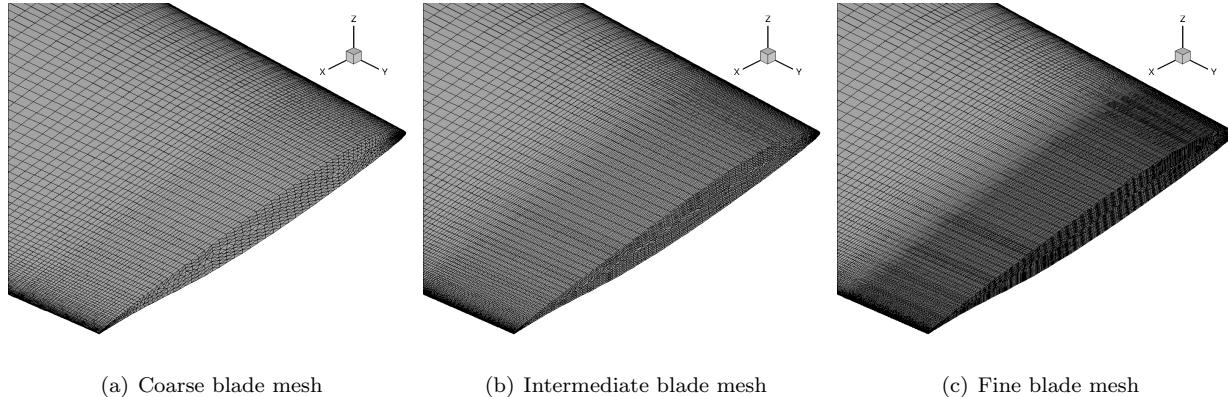


Figure 9. Blade mesh with different surface resolution for TRAM rotor.

Mesh System	C_T/σ	C_Q/σ	FM
“Coarse” mesh system	0.167405	0.018619	0.789600
“Intermediate” mesh system	0.167424	0.018617	0.789802
“Fine” mesh system	0.167464	0.018619	0.790012

Table 4. TRAM rotor performance with surface resolution.

forementioned resolution is used along the outboard 4% blade radius. This provides the necessary resolution to preserve the tip vortex as it moves inboard behind the blade. Figure 9 shows the surface mesh of the three cases. All the blade meshes extend to about half a tip chord distance from the blade. The wake spacing, which is the normal spacing at the strand outer boundary, is set to 2.5% of the chord length. For these set of calculations, the finest spacing in the off-body is set to twice the wake spacing in the strand grid. The three mesh systems considered here will be referred to as “coarse”, “intermediate” and “fine” mesh systems, respectively, in this section.

Table 4 shows the predicted thrust (C_T) and power (C_Q) coefficients (normalized by the rotor solidity, σ) as well as figure of merit (FM) for the three sets of simulations. Note that the tabulated data is obtained by averaging the integrated forces over the last rotor revolution. The thrust and power coefficients show less than 0.5% variation over the last rotor period. Consequently, the figure of merit show little more than 0.5% variation over this time period as seen in Figure 10. The unsteadiness in the prediction has a frequency of three per revolution, corresponding to the three blades in the rotor, indicating that the variations seen are inherent to the physics of the problem and not an artifact of the solution procedure. Temporal variations of similar magnitude were also observed in the forces predicted using

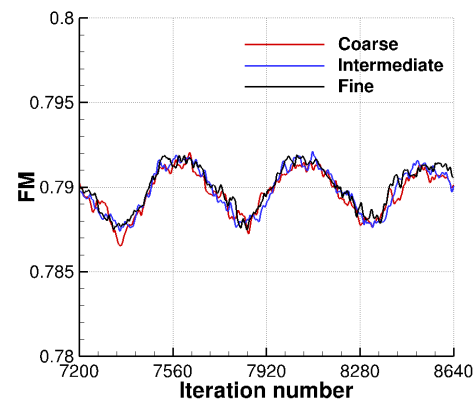


Figure 10. Time history of predicted figure of merit for TRAM rotor.

different mesh systems discussed later in the paper. Table 4 clearly shows that the rotor performance is not impacted much by the tip resolution and various quantities are almost identical in all the cases.

Figure 11 shows the vorticity magnitude contours near the tip of the blade for the three different cases. Also shown is a slice of the mesh to highlight the overset interface. The plot clearly shows the formation of tip vortex and its evolution from the near-body to the off-body grid. Careful observation shows that the vortex strength at the very early wake age is stronger for the finer blade meshes, but the strength of the vortex convecting downstream does not differ very much between the three mesh systems.

Figure 12 shows a quantitative comparison of vortex strength on the three different mesh systems by plotting the peak vorticity magnitude (normalized by the rotational frequency of the rotor) in the core of the vortex as a function of wake age. The wake age is defined to be 0° at the quarter-chord of the blade and it increases as one moves towards the trailing edge and beyond. The wake age at the trailing edge corresponds to 4.19° , which is highlighted in Fig. 12(a). Figure 12(a) shows the vortex strength till 12° wake age. From this figure, it is evident that the vortex strength initially grows till about mid-chord and it starts dropping thereafter. The strength predicted using a finer surface grid is definitely higher at the very early wake ages, but the predicted strengths using different meshes become comparable within a short-distance from the blade. From Fig. 12(b), it is evident that the strength predicted by all the three mesh systems are almost identical at later wake ages until a rotor revolution.

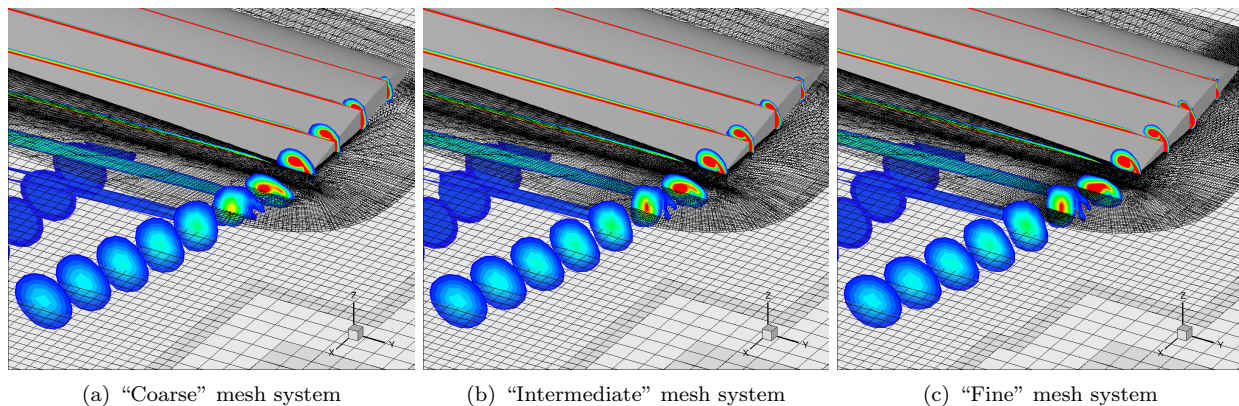


Figure 11. Vorticity contours near blade-tip for mesh systems with different surface resolution for TRAM rotor.

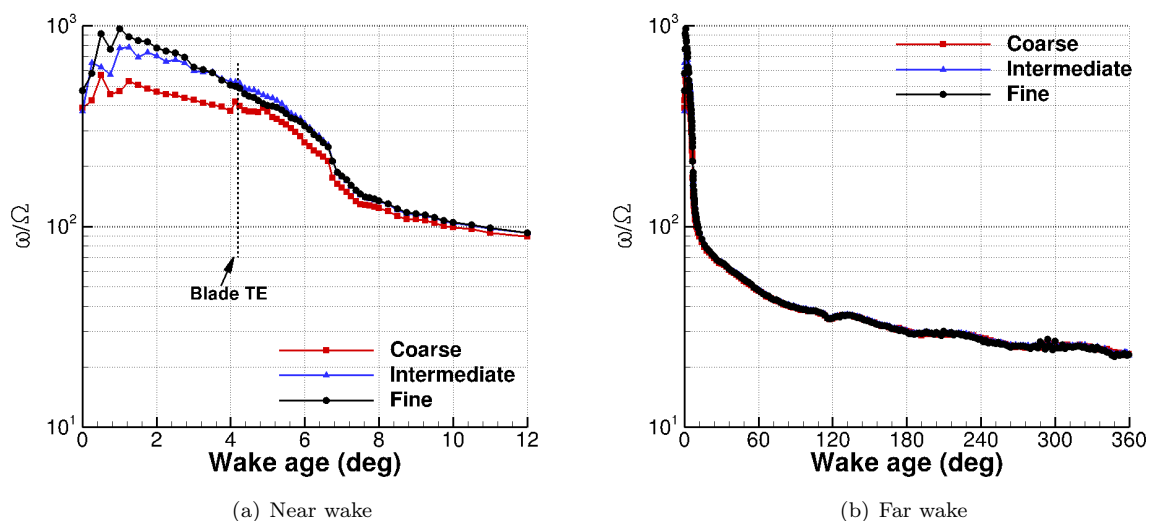


Figure 12. Peak vorticity magnitude in the vortex core as a function of wake age for mesh systems with different surface resolution for TRAM rotor.

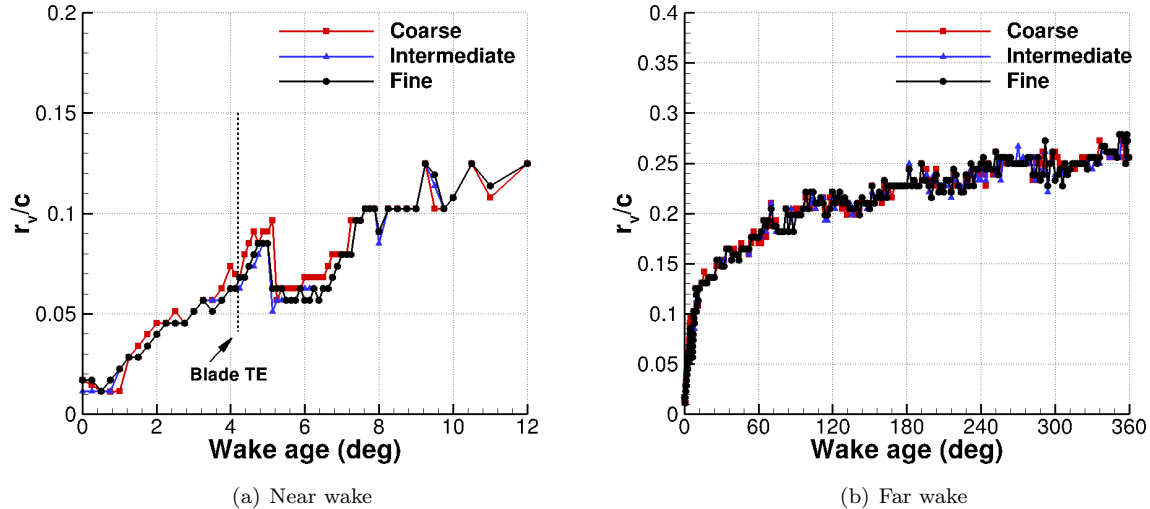


Figure 13. Vortex core radius as a function of wake age for mesh systems with different surface resolution for TRAM rotor.

Figure 13 shows the core radius, r_v , (normalized by the blade tip chord) as a function of wake age for all the cases. Core radius is measured as half the distance between peak-to-peak swirl velocity on a horizontal cut across the center of the vortex. The core radius is seen to grow for the most part, except for a small dip as the vortex goes past the blade tip. Meshes with the different surface resolutions predict very similar core radius everywhere including very close to the blade.

Figure 14 shows the visualization of the computed wake using iso-surface of Q-criterion colored by the vorticity magnitude for the three different simulations. The wake is very well resolved for a long period of time. The vortex is seen to be twisting at later wake ages. Comparing the plots using different mesh systems, there is no obvious qualitative difference in the predicted wake. The results presented in this section show that the surface resolution, particularly the resolution near the tip region, do not have a very significant impact on the rotor hover predictions. But, that is not to say that the surface mesh does not have to meet certain minimum quality required for a CFD calculation.

V.B. Strand Length

Next, the sensitivity of hover prediction to the outer extent of the strand mesh (strand length) is studied. The “rule-of-thumb” used for an overset calculation using a structured or an unstructured near-body grid in Helios is to have the near-body grid extend out about one chord away from the blade. However, such a recommendation does not hold true for the strand grid framework. Strand meshes have a tendency to fan out when extruded near convex regions of the surface such as near the blade trailing edge and tip. Limiting the outer extent of the strand mesh can prevent excessive grid fanning, and thus ensure sufficient resolution to evolve the tip vortex. Therefore, strand lengths of one tip chord or less are considered for this study. Three different blade meshes with short, intermediate and long strand lengths are used. These meshes use the same surface tessellation as the fine blade mesh described in the previous section. Also, the intermediate strand length blade mesh is identical to the fine blade mesh described in the previous section. Details regarding the strand length, number of strand points and the wake spacing of the three blade meshes is provided in Table 5. In the long strand length blade mesh, the normal spacing goes from the viscous spacing at the surface to 1.25% tip chord at quarter tip chord length, then increases to 2.5% chord at half chord length and then stays constant till the one chord outer boundary. The short and intermediate strand length meshes were generated by cutting back strand layers from the long mesh. The finest spacing used in the off-body is 5% tip chord, which means the mesh spacing ratio between the off-body and the near-body grid at the overset interface is 4:1 with the short strand length blade mesh and 2:1 with the intermediate and long strand length blade meshes. The resulting three mesh systems will be referred to as “short”, “intermediate” and “long”

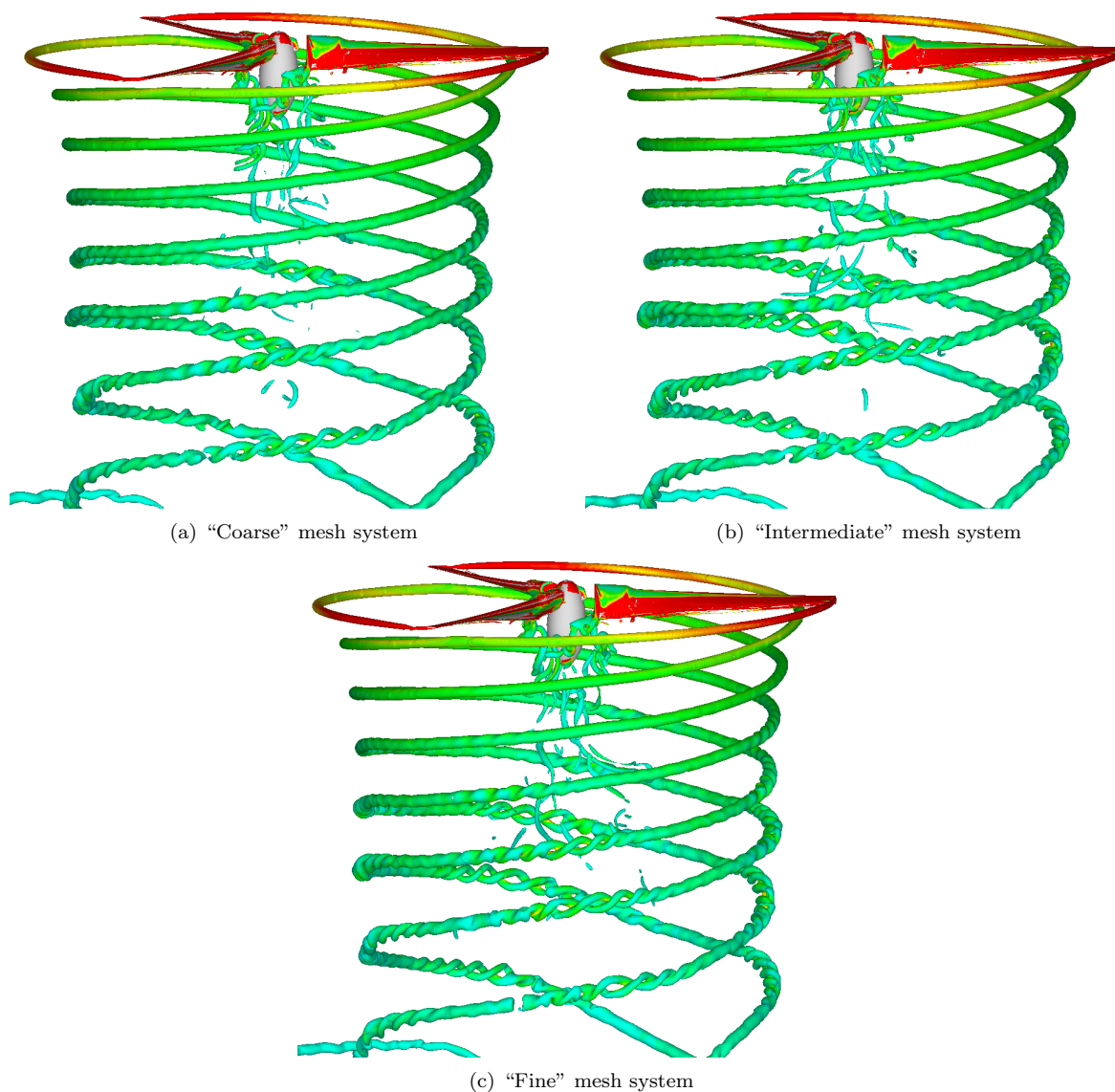


Figure 14. Iso-surfaces of Q -criterion for mesh systems with different surface resolution for TRAM rotor.

Mesh	Strand Length	Strand Points	Wake Spacing
Short strand length blade mesh	$0.25c$	83	$0.0125c$
Intermediate strand length blade mesh	$0.5c$	101	$0.025c$
Long strand length blade mesh	$1.0c$	125	$0.025c$

Table 5. TRAM blade grid statistics for mesh systems with different strand length. c is the tip chord.

mesh systems, respectively, in this and the following sections.

Table 6 shows the predicted thrust (C_T) and power (C_Q) coefficients (normalized by the rotor solidity, σ) as well as figure of merit (FM) for the three sets of simulations. While the “intermediate” and the “long” mesh systems predict similar rotor performance, the values predicted using the “short” mesh system show some disparity. Both the thrust and power predicted by the “short” mesh system is larger and the predicted FM is about 1% smaller, which is quite significant.

Figure 15 shows the vorticity magnitude contours near the tip of the blade for the three cases. Since all the

Mesh System	C_T/σ	C_Q/σ	FM
“Short” mesh system	0.168400	0.018924	0.783821
“Intermediate” mesh system	0.167464	0.018619	0.790012
“Long” mesh system	0.167400	0.018609	0.789982

Table 6. TRAM rotor performance for mesh systems with different strand length.

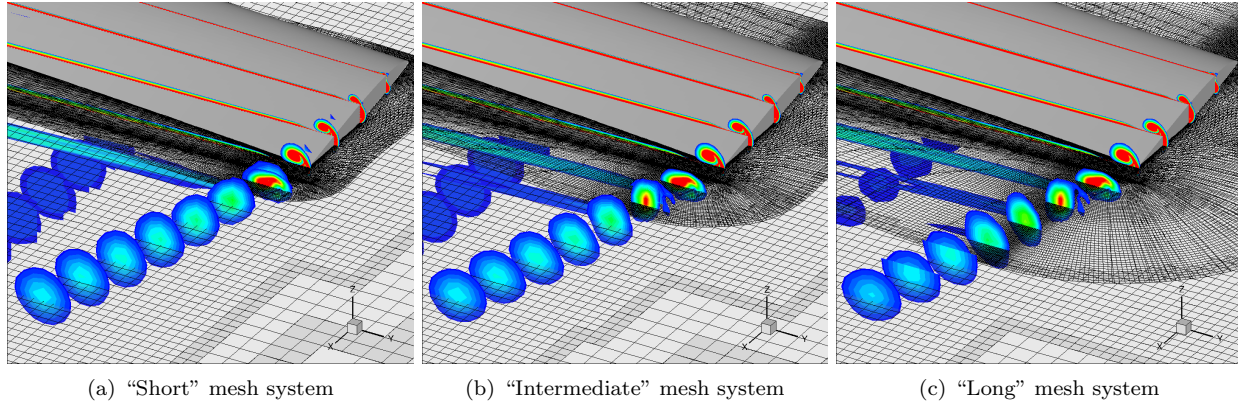


Figure 15. Vorticity contours near blade-tip for mesh systems with different strand length for TRAM rotor.

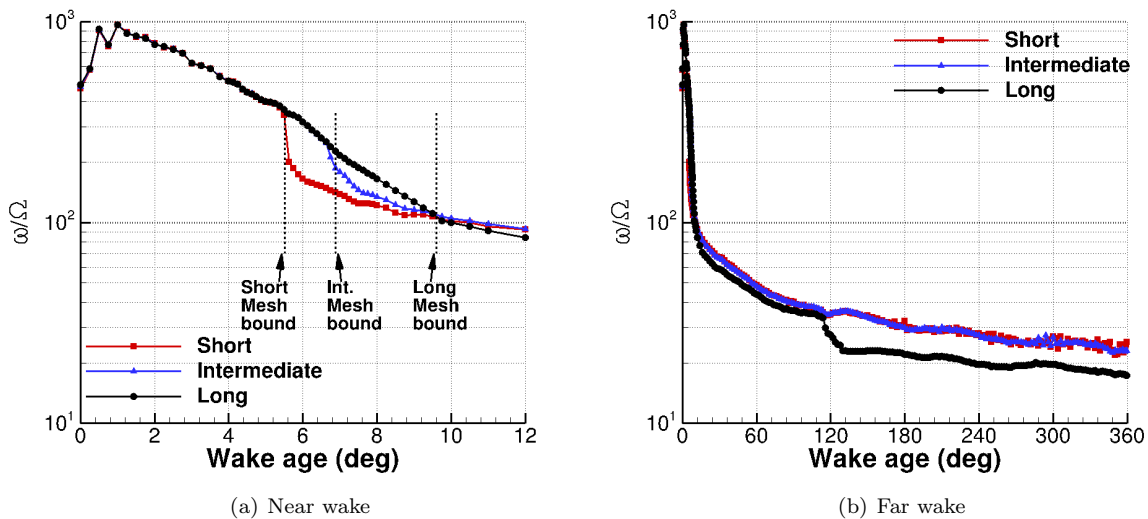


Figure 16. Peak vorticity magnitude in the vortex core as a function of wake age for mesh systems with different strand length for TRAM rotor.

blade meshes have identical surface resolution, there is no qualitative difference in the initial vortex roll-up predicted by various cases. The vortex in the “short” mesh system can be seen to dissipate very quickly at the overset interface due to larger than desirable off-body to near-body mesh spacing ratio. Figure 16(a) provides a quantitative estimate of drop in vortex strength by plotting the peak vorticity magnitude (normalized by the rotational frequency of the rotor) in the core of the vortex as a function of wake age. The plot marks the boundaries of various strand meshes and it is seen that the strength of the vortex drops more than 50% as it passes through the overset interface in the “short” mesh system. Loss of vortex strength at the overset interface is also observed in the “intermediate” and the “long” mesh systems, but the reduction in vortex strength is of smaller magnitude. When the vortex is transferred to the off-body mesh, it decays at a slower

rate as compared to in the near-body mesh. As a result, it is seen that the strength of the vortex at 12° wake age is comparable for the “short” and the “intermediate” mesh systems, while it is lower for the “long” mesh system. Figure 16(b) looks at the vortex strength with wake age for one rotor revolution. The vortex strength predicted by the “short” and “intermediate” mesh systems is very similar till the plotted wake age. However, the vortex strength predicted using the “long” mesh system is lower. The predicted strength is marginally lower till 120° , which corresponds to the first blade passage. A sharp drop in the vortex strength can be observed during the blade passage. At these instances, the vortex re-enters the long near-body grid at an inboard region, whereas it misses both the short and the intermediate length strand grids. Figure 17 shows a plot of vorticity magnitude identifying the returning vortex for the three mesh systems. The strand mesh is not refined sufficiently at an inboard station to convect strong vortices and therefore any re-entering vortex gets quickly dissipated. Differences can also be observed in the vortex core radius, r_v , (normalized by the blade tip chord) plotted in Fig. 18. While the core radius predicted by the “short” and “intermediate” mesh systems is very similar at wake ages going from 12° to 360° , the “long” mesh system predicts a much larger core radius. At regions very close to the blade, the core radius predicted by all three meshes have disparities that is consistent with the vortex strength prediction.

Figure 19 shows the visualization of the computed wake using iso-surface of Q-criterion colored by vorticity magnitude for the three different simulations. The wake location predicted by all the mesh systems is very

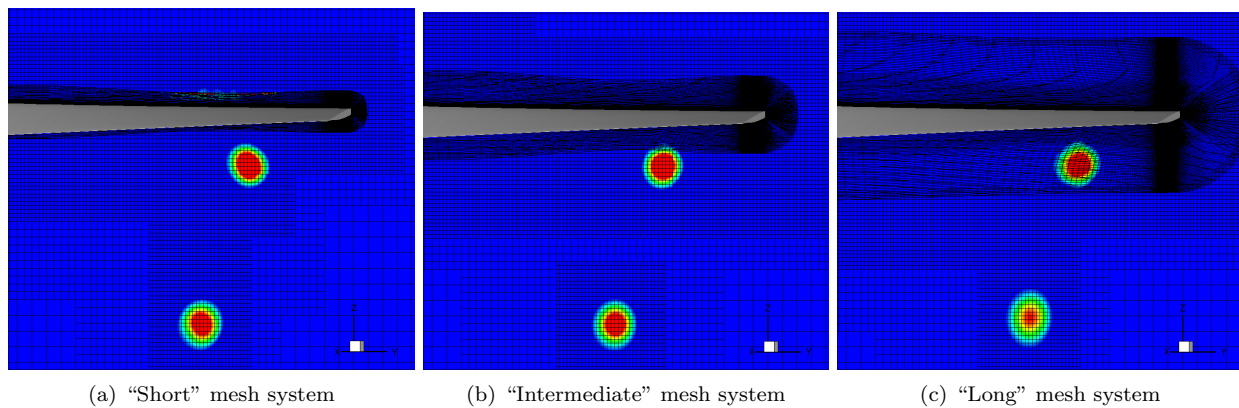


Figure 17. Vorticity magnitude showing returning vortex for mesh systems with different strand length for TRAM rotor.

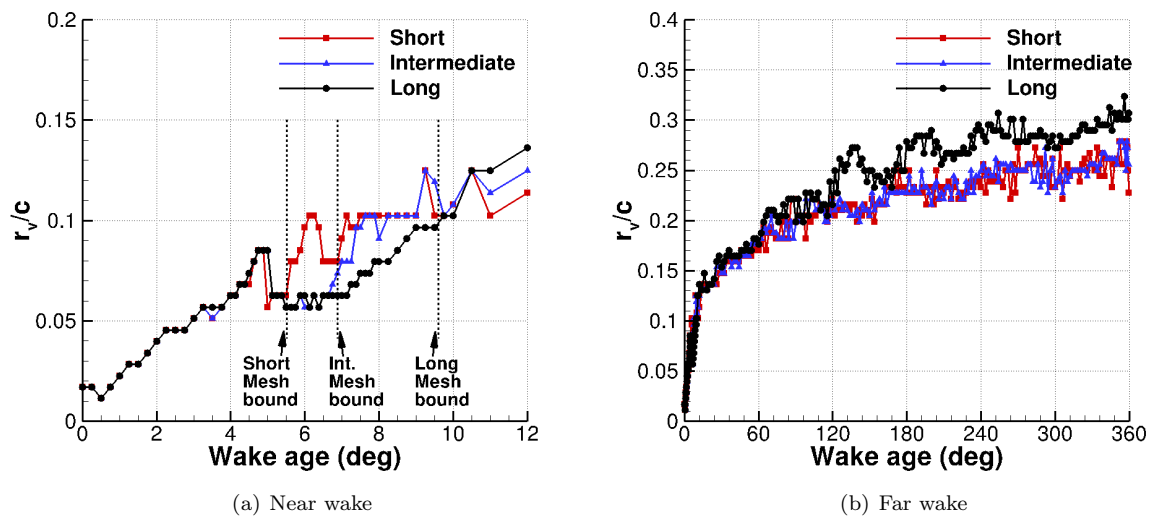


Figure 18. Vortex core radius as a function of wake age for mesh systems with different strand length for TRAM rotor.

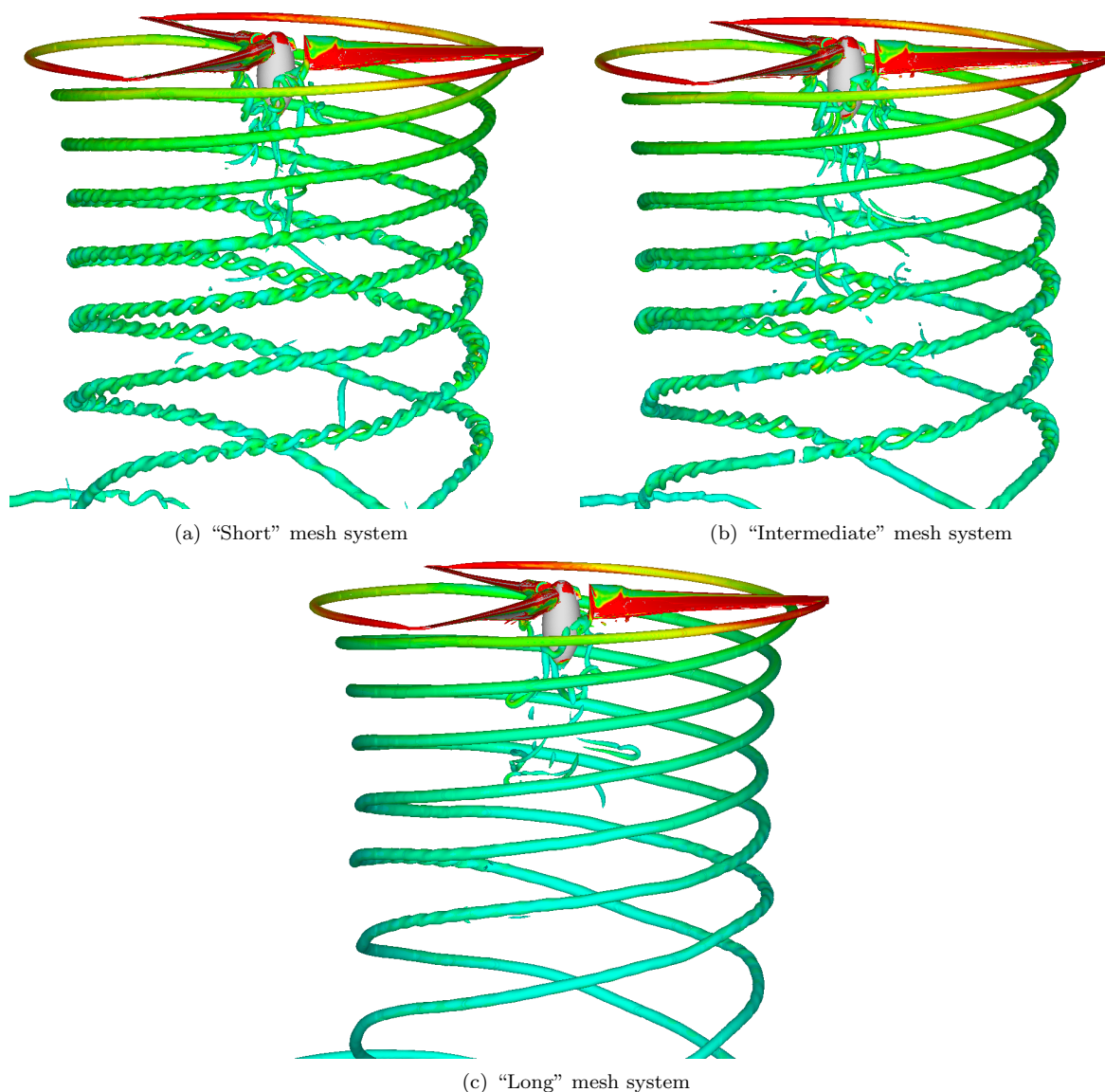


Figure 19. Iso-surfaces of Q -criterion for mesh systems with different strand length for TRAM rotor.

similar, however the wake structure is not. The instabilities in the wake is seen to reduce as the strand length increases.

Overall, it can be summarized that the hover predictions are very sensitive to the strand length, if finest the off-body Cartesian mesh refinement level is kept the same. Using strand mesh that goes out to only quarter of the tip chord will have a smaller wake spacing and therefore, introduces large discrepancy between the strand and the Cartesian mesh resolution. This leads to incorrect near-wake prediction, which in turn has significant impact on the rotor performance prediction. On the other hand, having a strand length equal to one tip chord not only dissipates the tip vortex in the early wake ages due to grid fanning, but also cannot preserve the returning vortex re-entering the near-body mesh. Using half a tip chord strand length seems to provide the best result in terms of both the performance as well as wake prediction.

V.C. Cartesian Mesh Resolution

It is clear from the previous section that poor grid resolution matching at the overset interface can significantly impact the hover predictions. In this section, the effect of off-body Cartesian mesh resolution is investigated. The short and intermediate strand length blade meshes from the previous section are simulated with a finer

off-body Cartesian mesh, obtained by halving the finest mesh spacing. This provides a mesh spacing ratio between the off-body and the near-body grid of 2:1 for the short strand length blade mesh and 1:1 for the intermediate strand length blade mesh at the overset interface. The two new mesh systems considered here will henceforth be referred to as “short - fine Cart” and “intermediate - fine Cart” mesh systems. Table 7 provides the details of the finest Cartesian spacing and final number (varies during the simulation due to adaption) of Cartesian grid points in different mesh systems. Refining the Cartesian mesh nearly doubles the mesh size. Also, note that using different near-body blade meshes with identical off-body refinement level produces similar Cartesian mesh point count.

Mesh System	Finest Cartesian Spacing	Number of Cart. Points (millions)
“Short” mesh system	0.05c	100.6
“Intermediate” mesh system	0.05c	90.1
“Short - fine Cart” mesh system	0.025c	170.9
“Intermediate - fine Cart” mesh system	0.025c	176.5

Table 7. TRAM Cartesian mesh statistics for different mesh systems. c is the tip chord.

Table 8 shows the predicted thrust (C_T) and power (C_Q) coefficients (normalized by the rotor solidity, σ) as well as figure of merit (FM) for the simulations performed on different mesh systems. The results from the “short” and the “intermediate” mesh systems are the same as shown in the previous section. From the table, refining the Cartesian mesh is clearly seen to impact the rotor performance prediction. The figure of merit predicted using finer Cartesian mesh is about 0.5% larger, signifying the need to accurately resolve the tip vortex evolution. When the Cartesian mesh is refined, the performance predicted using the short strand length blade mesh is comparable to the one with the intermediate strand length blade mesh, clearly indicating the need to have good off-body to near-body grid spacing ratio.

Mesh System	C_T/σ	C_Q/σ	FM
“Short” mesh system	0.168400	0.018924	0.783821
“Intermediate” mesh system	0.167464	0.018619	0.790012
“Short - fine Cart” mesh system	0.168098	0.018611	0.794863
“Intermediate - fine Cart” mesh system	0.168018	0.018616	0.794082

Table 8. TRAM rotor performance for mesh systems with different Cartesian mesh resolution.

Figure 20 shows the vorticity magnitude contours near the tip of the blade for the two mesh systems using finer Cartesian refinement. Similar contours for the “short” and “intermediate” mesh systems were plotted in Figs. 15(a) and (b), respectively. The transfer of vortex from the near-body to the off-body mesh is much smoother with the refined Cartesian mesh. The vortex strength is also maintained well in the off-body mesh while using a finer resolution. Figure 21 shows the evolution of peak vorticity magnitude (normalized by the rotational frequency of the rotor) in the core of the vortex as a function of wake age. There is no visible reduction in vortex strength at the overset interface when using a finer Cartesian mesh. The off-body solver uses a high-order spatial discretization and therefore, can better preserve the vortex better as compared to the near-body solver operating on grids with similar resolution. Owing to this, the near wake vortex strength predicted by the “short - fine Cart” mesh system is higher than that predicted by the “intermediate - fine Cart” mesh system. In the “short - fine Cart” mesh system, the vortex is transferred to the off-body grid at an earlier wake age. From Fig. 21(b), it is evident that the vortex strength on the “short - fine Cart” mesh system is higher for about two blade passages (240° wake age), but due to a slightly faster strength decay (possible caused by larger wake instability as discussed later), it becomes comparable to the strength predicted by the “intermediate - fine Cart” mesh system by the wake age of 360° . The vortex strength predicted by using a finer Cartesian mesh is significantly larger than that computed using a coarser mesh even after one revolution. Figure 22 shows the core radius, r_v , (normalized by the blade tip chord) as a function of wake age for all the cases. The use of finer Cartesian mesh clearly predicts a much tighter vortex core. The predicted core radius does not change with the varying extent of the near-body mesh.

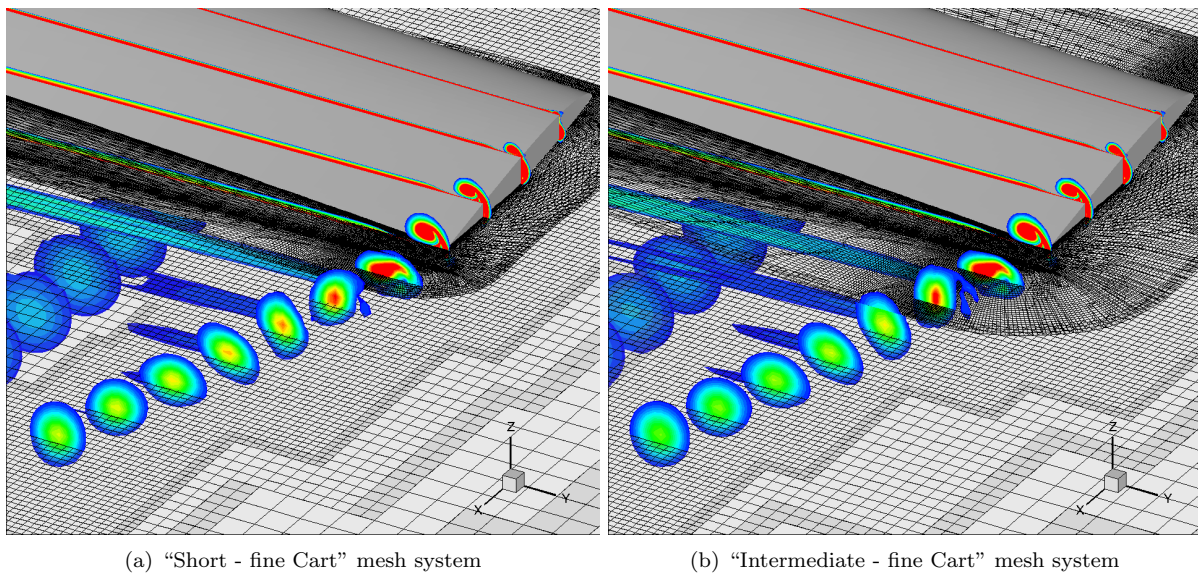


Figure 20. Vorticity contours near blade-tip for mesh systems with finer Cartesian mesh resolution for TRAM rotor.

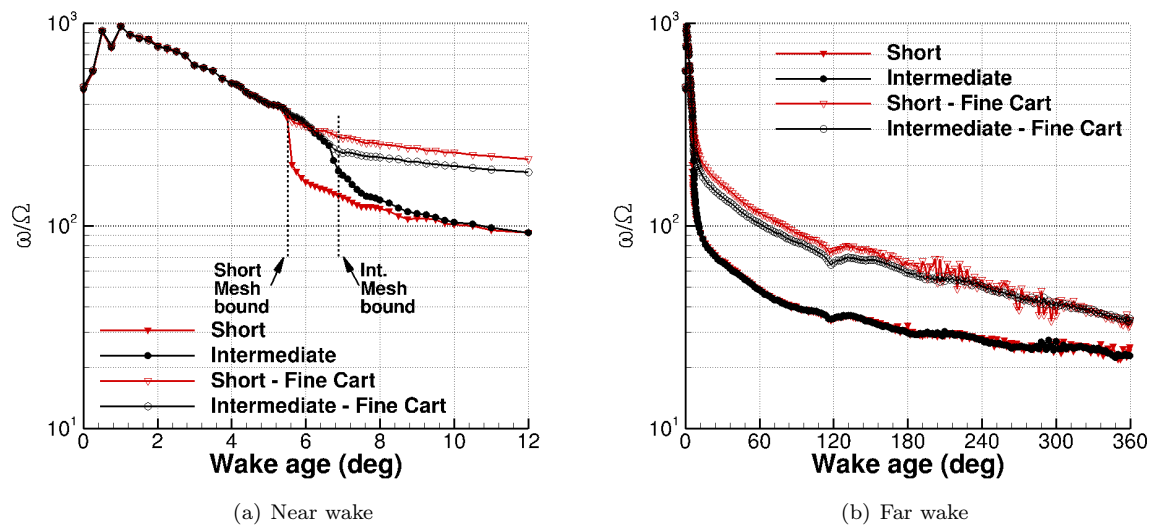


Figure 21. Peak vorticity magnitude in the vortex core as a function of wake age for mesh systems with different Cartesian mesh resolution for TRAM rotor.

Figure 23 shows the visualization of the computed wake using iso-surface of Q -criterion colored by vorticity magnitude for the two new mesh systems. When compared to Fig. 19, the predicted vortex trajectory does not change when Cartesian mesh is refined. Surprisingly, the use of finer Cartesian mesh is seen produce a more stable wake. The wake predicted by the “short - fine Cart” mesh system shows slightly more instability when compared to that predicted using “intermediate - fine Cart” mesh system.

To summarize this section, refining the Cartesian mesh is seen to improve the overall hover predictions, both in terms of performance as well as wake characteristics. With sufficient Cartesian mesh refinement, there is no practical difference in the results when using a strand mesh extending either to quarter chord or to half chord distance. Additional simulations with even finer off-body mesh is needed to determine if the use of shorter blade mesh has any clear advantage over the intermediate length mesh. Such a calculation is very expensive and may not be of any practical value. Therefore, use of strand grid with half a chord extent is recommended for most rotor blade simulations.

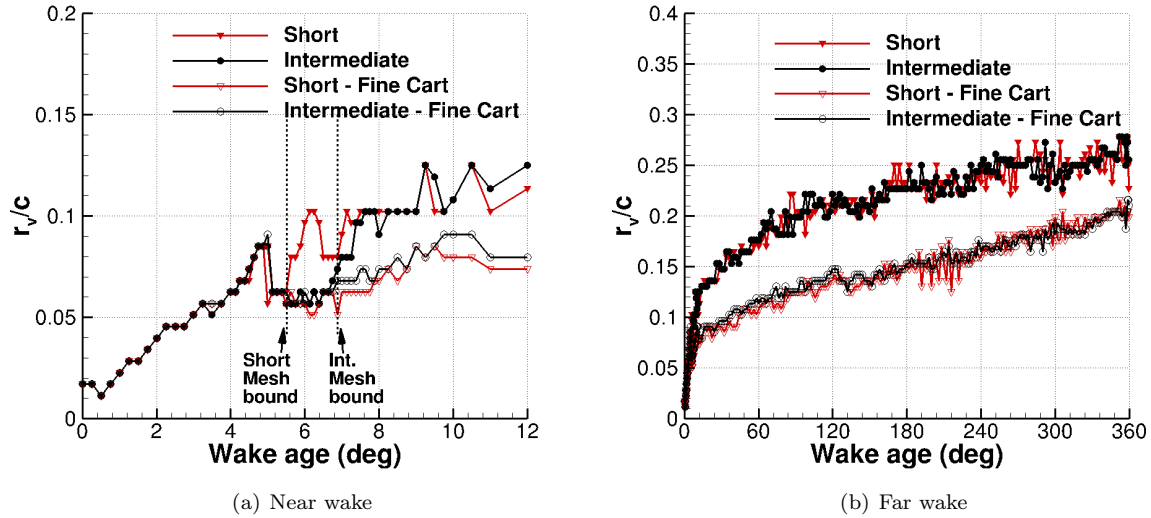


Figure 22. Vortex core radius as a function of wake age for mesh systems with different Cartesian mesh resolution for TRAM rotor.

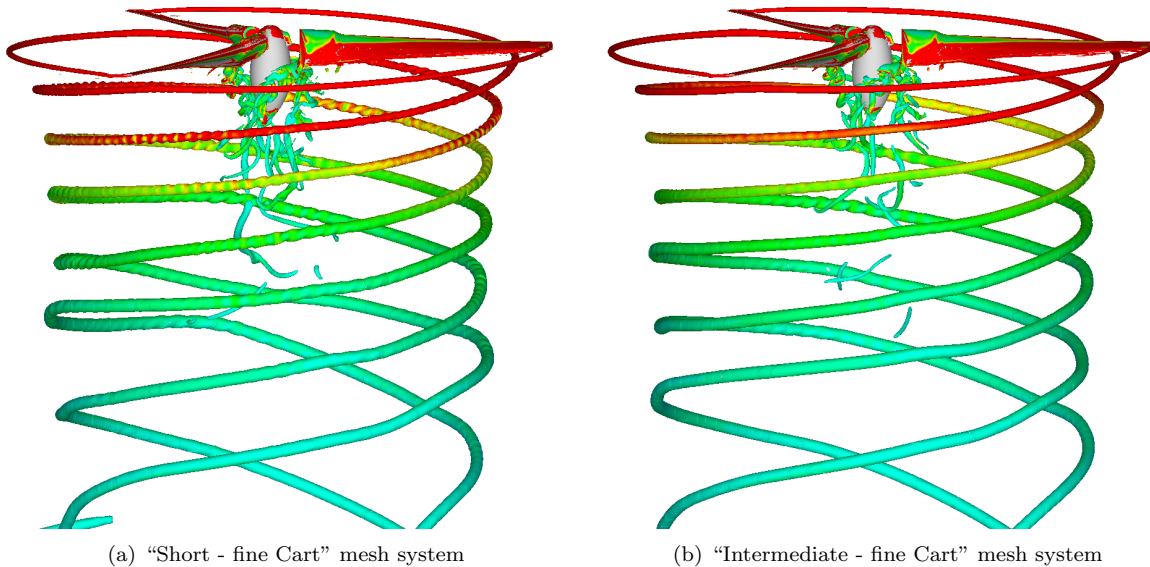


Figure 23. Iso-surfaces of Q-criterion for mesh systems with finer Cartesian mesh resolution for TRAM rotor.

VI. Concluding Remarks

The strand grid framework is being pursued by HPCMP CREATETM program as a viable approach to achieve automatic viscous mesh generation. Strand grid generation require very few input parameters. This work investigates the sensitivity of rotor hover predictions to various meshing parameters in the the strand grid framework using the hovering TRAM rotor calculations at 14° collective angle. The sensitivity to surface mesh resolution, outer extent of the strand grid (strand length) and the resolution of the off-body Cartesian mesh is explored. Details of the performance and the wake characteristics predictions are presented. Listed below are the specific conclusions.

1. Surface resolution, when ascertained a minimum quality needed for a CFD calculation, does not have any significant impact on rotor hover predictions. The strand mesh with only 10 points across the thickness of the blade predicts a weaker vortex during the initial roll-up, but the vortex strength

quickly recovers and results become comparable to the meshes having 20 or 40 points across the blade thickness.

2. Hover predictions are very sensitive to the strand length, if the finest off-body Cartesian mesh refinement level is left unchanged. Using a short strand length, resulting in poor near-body to off-body overlap resolution, predicts incorrect rotor performance due to errors introduced in transferring the solution at the overset interface. On the other hand, using a long strand mesh dissipates the near wake due to grid fanning and the returning vortex because it re-enters a coarse portion of the near-body grid. Using half a tip chord strand length seems to provide the best result in terms of both the performance as well as the wake prediction.
3. Refining the Cartesian mesh to have a mesh resolution comparable to the near-body strand grid is seen to improve the overall hover predictions, both in terms of performance as well as wake characteristics. But, any additional level of refinement comes with a penalty of almost doubling the computation cost of the off-body solution. With sufficient Cartesian mesh refinement, there is no practical difference in the results using a strand mesh extending either to quarter chord or to half chord distance. But, the use of shorter strand mesh requires a finer Cartesian mesh to ensure good overset interfacing and cannot be used with a coarser off-body mesh. Therefore, use of strand grid with half a chord extent is probably the best for most rotor blade simulations. The ratio of the off-body to the near-body grid spacing at the overset interface should be determined based on the available resources and the importance of interactional aerodynamics in the problem.

Acknowledgments

Material presented in this paper is a product of the CREATE-AV Element of the Computational Research and Engineering for Acquisition Tools and Environments (CREATE) Program sponsored by the U.S. Department of Defense HPC Modernization Program Office.

References

- ¹Chaderjian, N. M., and P. G. Buning, "High Resolution Navier-Stokes Simulation of Rotor Wakes," American Helicopter Society 67th Annual Forum, Virginia Beach, VA, May 3–5, 2011.
- ²Lee-Rauch, E. M., Biedron, R. T., "Simulation of an Isolated Tiltrotor in Hover with an Unstructured Overset-Grid RANS Solver," American Helicopter Society 65th Annual Forum, Grapevine, TX, May 2009.
- ³Wissink, A. M., Potsdam, M., Sankaran, V., Sitaraman, J., Mavriplis, D., "A Dual-Mesh Unstructured Adaptive Cartesian CFD Approach for Hover Prediction," *Journal of the American Helicopter Society*, Vol. 61, No. 1, Jan 2016, pp. 1–19(19).
- ⁴Hariharan, N. "Helicopter Aerodynamic Modeling of S-76 Rotor with Tip-Shape Variations: Review of AIAA Standardized Hover Evaluations," AIAA-2016-0031, 54th AIAA Aerospace Sciences Meeting, San Diego, Jan 2016.
- ⁵Meakin, R., Wissink, A., Chan, W., Pandya, S., and Sitaraman, J., "On Strand Grids for Complex Flows," AIAA-2007-3834, 18th AIAA Computational Fluid Dynamics Conference, Miami, FL, June 2007.
- ⁶Katz, A., Wissink, A., Sankaran, V., Meakin, R., and Chan, W. "Application of Strand Meshes to Complex Aerodynamic Flowfields," *Journal of Computational Physics*, Vol. 230, No. 17, 2011.
- ⁷Wissink, A., Jayaraman, B., Datta, A., Sitaraman, J., Potsdam, M., Kamkar, S., Mavriplis, D., Yang, Z., Jain, R., Lim, J., and Strawn, R., "Capability Enhancements in Version 3 of the Helios High-Fidelity Rotorcraft Simulation Code," AIAA-2012-0713, 50th AIAA Aerospace Sciences Meeting, Nashville, TN, January 2012.
- ⁸Sankaran, V., A. Wissink, A. Datta, J. Sitaraman, B. Jayaraman, M. Potsdam, A. Katz, S. Kamkar, B. Roget, H. Saberi, W. Chen, W. Johnson, and R. Strawn, "Overview of the Helios Version 2.0 Computational Platform for Rotorcraft Simulations," AIAA-2011-1105, 49th AIAA Aerospace Sciences Meeting, Orlando FL, Jan 2011.
- ⁹Sankaran, V., J. Sitaraman, A. Wissink, A. Datta, B. Jayaraman, M. Potsdam, D. Mavriplis, Z. Yang, D. O'Brien, H. Saberi, R. Cheng, N. Hariharan, and R. Strawn, "Application of the Helios Computational Platform to Rotorcraft Flowfields," AIAA-2010-1230, 48th AIAA Aerospace Sciences Meeting, Orlando FL, Jan 2010.
- ¹⁰Post, D., "A new DoD initiative: the Computational Research and Engineering Acquisition Tools and Environments (CREATE) program," *Journal of Physics*, Conference Series 125, 2008.
- ¹¹Lakshminarayan, V. K., Sitaraman, J., Roget, B., and Wissink, A. M., "Development and Validation of a Multi-Strand Solver for Complex Aerodynamic Flows," AIAA paper-2016-1581, 54th Aerospace Sciences Meeting, San Diego, CA, January 4-8, 2016.
- ¹²Sitaraman, J., Floros, M., Wissink, A., and Potsdam, M., "Parallel domain connectivity algorithm for unsteady flow computations using overlapping and adaptive grids," *Journal of Computational Physics*, Vol. 229, No. 12, pp. 4703–4723, 2010.
- ¹³Wissink, A., Sitaraman, J., Sankaran, V., Mavriplis, D., and Pulliam, T., "A Multi-Code Python-Based Infrastructure for Overset CFD with Adaptive Cartesian Grids", AIAA-2008-0927, 46th AIAA Aerospaces Conference, Reno, NV, January 2008.

- ¹⁴Sitaraman, J., Katz, A., Jayaraman, B., Wissink, A., and Sankaran, V., "Evaluation of a Multi-Solver Paradigm for CFD using Unstructured and Structured Adaptive Cartesian Grids," AIAA-2008-0660, 46th AIAA Aerospaces Conference, Reno, NV, January 2008.
- ¹⁵Roe, P.L., "Approximate Riemann Solvers, Parameter vectors, and Difference Schemes," *Journal of Computational Physics*, Vol. 43, pp. 357–372, 1981.
- ¹⁶Van Albada, G., Van Leer, B., and Roberts, W., "A comparative study of computational methods in cosmic gas dynamics," *Astronomy and Astrophysics* Vol. 108, pp. 76-84, 1982.
- ¹⁷Spalart, P., and Allmaras, S., "A one-equation turbulence model for Aerodynamic flows," *Le Recherche Aérospatiale*, Vol. 1, pp. 5–21, 1994.
- ¹⁸Saad, Y., and Schultz, M., "GMRES: a generalized minimal residual algorithm for solving nonsymmetric linear systems," *SIAM Journal on Scientific and Statistical Computing*, Vol. 7, No. 3, pp. 856–869, 1986.
- ¹⁹Karypis, G. and Kumar, V., "A Fast and Highly Quality Multilevel Scheme for Partitioning Irregular Graphs," *SIAM Journal on Scientific Computing*, Vol. 20, No. 1, pp. 359-392, 1999.
- ²⁰Wissink, A. M., R. D. Hornung, S. R.Kohn. S. S. Smith, and N. S. Elliott, "Large Scale Structured AMR Calculations Using the SAMRAI Framework," SC01 Proceedings, Denver, CO, November 2001.
- ²¹Wissink, A.M., Sitaraman, J., B. Jayaraman, Roget, B., Lakshminarayan, L., M. Potsdam, R. Jain, J. Leffel, J. Forsythe, A. Bauer, "Recent Advancements in the Helios High-Fidelity Rotorcraft Simulation Code," AIAA-2016-0563, 54th AIAA Aerospace Sciences Meeting, San Diego, Jan 2016.
- ²²Leffel, J., Sitaraman, J., Lakshminarayan, V., and Wissink, A., "Towards Efficient Parallel-in-Time Simulation for Periodic Flows," AIAA-2016-0066, 54th Aerospace Sciences Meeting, San Diego, CA, January 2016.
- ²³Wissink, M., Sitaraman, J., Katz, A., and Roget, B. "Application of 3D Strand Mesh Technology to Rotorcraft Hover," AIAA-2015-0044, 53rd AIAA Aerospace Sciences Meeting, Kissimmee, FL, January 2015.
- ²⁴Berger, M. J., and P. Colella, "Local Adaptive Mesh Refinement for Shock Hydrodynamics," *J. Comp. Phys.*, **82**, 1989, pp. 65–84.
- ²⁵Kamkar, S. J., A.M. Wissink, V. Sankaran, A. Jameson, "Feature-Driven Cartesian Adaptive Mesh Refinement for Vortex-Dominated Flows," *Journal of Computational Physics*, Vol. 230, No. 16, July 2011, pp. 6271-6298.
- ²⁶Johnson, W., "Calculation of Tilt Rotor Aeroacoustic Model (TRAM DNW) Performance, Airloads, and Structural Loads," AHS Aeromechanics Specialists' Conference, Atlanta, GA, Nov. 2000.
- ²⁷Mavriplis, D., and Mani, K., "Unstructured Mesh Solution Techniques using the NSU3D Solver," AIAA Paper 2014-0081, 52nd AIAA Aerospace Sciences Conference, National Harbor, MD, January 2014.
- ²⁸Wissink, A., "Investigation of Dual Mesh CFD Approach for Hover," 5th Decennial AHS Aeromechanics Specialists' Conference, San Francisco, CA, January 2014.
- ²⁹Martin, P., Pugliese, G., and Leishman, J., "High Resolution Trailing Vortex Measurements in the Wake of a Hovering Rotor," *Journal of the American Helicopter Society*, Vol. 49, No. 1, pp. 39–52, 2003.